A Revised Conceptual Model of the Tropical Marine Boundary Layer. Part I: Statistical Characterization of the Variability Inherent in the Wintertime Trade Wind Regime over the Western Tropical Atlantic

JENNIFER L. DAVISON, ROBERT M. RAUBER, AND LARRY DI GIROLAMO

Department of Atmospheric Sciences, University of Illinois at Urbana–Champaign, Urbana, Illinois

MARGARET A. LEMONE

National Center for Atmospheric Research, Boulder, Colorado

(Manuscript received 21 November 2012, in final form 19 April 2013)

ABSTRACT

This paper investigates wintertime tropical marine boundary layer (TMBL) statistical characteristics over the western North Atlantic using the complete set of island-launched soundings from the Rain in Cumulus over the Ocean (RICO) experiment. The soundings are subdivided into undisturbed and disturbed classifications using two discriminators: 1) dates chosen by Global Energy and Water Cycle Experiment (GEWEX) Cloud System Studies (GCSS) investigators to construct the mean RICO sounding and 2) daily average rain rates.

A wide range of relative humidity (RH) values was observed between the surface and 8.0 km. At 2.0 km, half the RH values were within 56%–89%; at 4.0 km, half were within 13%–61%. The rain-rate method of separating disturbed and undisturbed soundings appears more meaningful than the GCSS method. The median RH for disturbed conditions using the rain-rate method showed moister conditions from the surface to 8.0 km, with maximum RH differences of 30%–40%. Moist air generally extended higher on disturbed than undisturbed days.

Based on equivalent potential temperature, wind direction, and RH analyses, the most common altitude marking the TMBL top was about 4.0 km. Temperature inversions (over both 50- and 350-m intervals) were observed at every altitude above 1.2 km; there were no dominant inversion heights and most of the inversions were weak. Wind direction analyses indicated that winds within the TMBL originated from more tropical latitudes on disturbed days.

The analyses herein suggest that the RICO profile used to initialize many model simulations of this environment represents only a small subset of the broad range of possible conditions characterizing the wintertime trades.

1. Introduction

The equilibrium structure of the tropical marine boundary layer (TMBL) and the role of shallow convection in TMBL energy and moisture budgets have been well established as a result of a half century of study using observations and theoretical, large-eddy, and general circulation modeling [see pioneering work of Malkus (1958); seminal papers in the 1980s by Betts (e.g., Betts and Albrecht 1987; Betts and Ridgway 1988); and more recent reviews by Betts (1997), Siebesma (1998), Stevens (2005, 2006), Neggers et al. (2006), and Stevens and Brenguier (2009)]. As summarized by Stevens (2006) using observations from one flight during the Rain in Cumulus over the Ocean (RICO) experiment (Fig. 1, reproduced from his Fig. 5) and Neggers et al. (2006, their Fig. 1), the trade wind boundary layer can be broadly characterized in terms of two layers, a well-mixed subcloud layer with an internal characteristic time scale for mixing on the order of 15 min, and a poorly mixed cumulus cloud layer with the time scale for mixing ranging from 8 h near cloud base to over 1 day at the trade wind inversion (Betts 1997). The TMBL is topped by a free-tropospheric dry layer extending from the trade wind inversion to the tropopause. Within the TMBL, two thin layers mark the boundaries between the primary layers. The first thin layer, called the transition layer, typically contains very shallow clouds. The second thin layer caps the taller trade wind cumuli and

Corresponding author address: Jennifer L. Davison, Department of Atmospheric Sciences, University of Illinois at Urbana–Champaign, 105 S. Gregory St., Urbana, IL 61801.
E-mail: jdavison@earth.uiuc.edu

DOI: 10.1175/JAS-D-12-0321.1

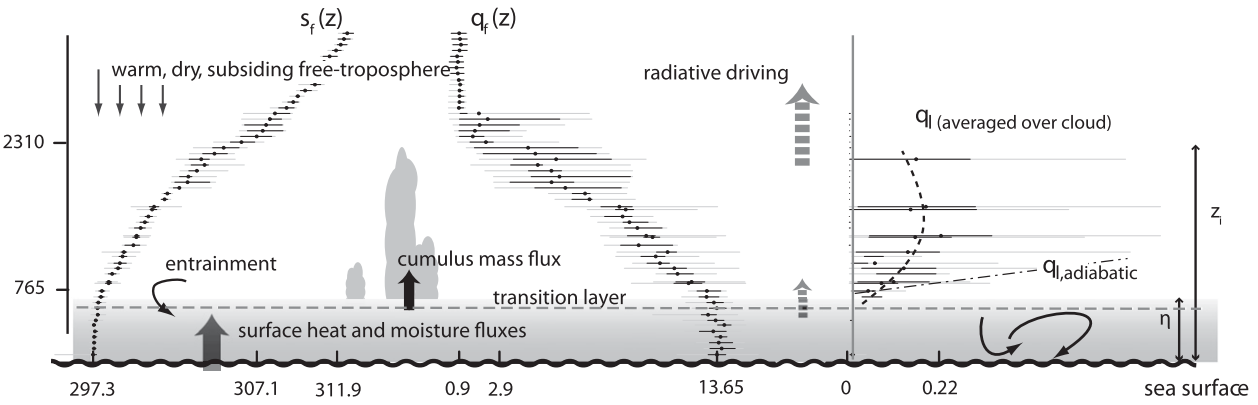

FIG. 1. Structure of the cumulus-topped boundary layer as observed during the tenth research flight of RICO. The *y* axis shows the top of the cloud layer and the LCL of the mean surface layer air in meters. The values on the *x* axis give (left) the ratio of the liquid-water static energy to the specific heat at constant pressure (s/c_p), averaged over the subcloud layer at 2300 and at 3500 m; (middle) the specific humidity q at 3500 and 2300 m, and averaged over the subcloud layer; and (right) the liquid-water specific humidity q_l over cloud passes only (where cloud coverage is typically 5%–10%). Basic processes determining the thermodynamic structure of the cloud and subcloud layers are indicated schematically. The thermodynamic profiles are constructed from the entirety of the flight data: gray lines show range, black lines show interquartile spread, and dots show median values. From Stevens (2006).

is often referred to as the trade wind inversion layer. Budget studies have shown that the TMBL mean state arises from a balance between surface heat and moisture fluxes, dry and moist convective transport, radiation, large-scale subsidence, and horizontal transport by the large-scale flow (e.g., Riehl et al. 1951; Yanai et al. 1973; Nitta and Esbensen 1974).

A key factor controlling the thermodynamic and dynamic state of the TMBL is the distribution of water vapor. Measurements of water vapor are integral to understanding both weather and climate processes. Water vapor is critical in determining when and where moist convection is initiated, how long clouds persist, and the amount and distribution of precipitation. Additionally, water vapor is a strong absorber of infrared radiation and is responsible for nearly 60% of the clear-sky greenhouse effect (Trenberth et al. 2007). According to Kim and Ramanathan (2008), water vapor accounts for two-thirds of the infrared radiation absorbed by the atmosphere under clear-sky conditions. Lack of knowledge of the water vapor distribution at sufficient temporal and spatial resolution is one of the limiting factors in improving weather forecasts (e.g., Weckwerth et al. 2004; Roberts et al. 2008).

Campaigns carried out in the trade wind regime have characterized the mean state of the TMBL based on soundings or averages derived from aircraft flight legs. Averaged or composited profiles from these campaigns have been used to determine representative heights at which key layers occur (e.g., Malkus 1958; Betts and Albrecht 1987; Kloesel and Albrecht 1989; Yin and Albrecht 2000) and to contrast structural differences between various trade wind regimes [e.g., dry versus rainy (Nuijens et al. 2009), clear versus partly cloudy (Pennell and LeMone 1974), transition layer versus no transition layer (Yin and Albrecht 2000), and q reversal versus no q reversal, where their q is mixing ratio (Kloesel and Albrecht 1989)].

Studies carried out over the western tropical North Atlantic Ocean have culminated in a series of averaged thermodynamic and moisture profiles that have served as the initial state for the vast majority of large-eddy simulations (LESs) and column model simulations of the western Atlantic trade wind environment [e.g., Pennell and LeMone 1974; see LES studies by Sommeria and LeMone (1978) and Cuijpers and Duynkerke (1993); Barbados Oceanographic and Meteorological Experiment (BOMEX) Phase I (Stevens et al. 2001); BOMEX Phase III (Siebesma et al. 2003); RICO (vanZanten et al. 2011)]. Each representative profile used in these modeling studies was generated by averaging profiles from a subset of the experimental days during which the environment was characterized as ''undisturbed.'' These simulations have been used, for example, to quantify fractional entrainment and detrainment rates of trade wind cumuli (Siebesma and Cuijpers 1995; Siebesma and Holtslag 1996; Neggers et al. 2002; de Roode and Bretherton 2003; de Rooy and Siebesma 2008); determine aerosol effects on clouds, precipitation, and the organization of shallow convection (Xue and Feingold 2006; Xue et al. 2008); examine the controls on size statistics of shallow cumulus (Neggers et al. 2003); and develop parameterizations for GCMs (e.g., von Salzen and McFarlane 2002; Berg and Stull 2005). The expression ''conceptual model of the tropical marine boundary layer,'' in this series of papers,

refers to the idealized structure of the trade wind environment as characterized by the thermodynamic, moisture, and wind profiles used to initiate these past model simulations.

Undisturbed conditions in the trades are generally characterized in all seasons by small nonprecipitating cumuli. However, the character of ''disturbed'' conditions depends upon both season and geographic location. For example, during the Global Atmospheric Research Program (GARP) Atlantic Tropical Experiment (GATE), which occurred in the eastern tropical North Atlantic during the 1974 hurricane season, the disturbed conditions consisted of deep tropospheric convection often organized in squall lines that produced between 25 and 50 mm of rainfall during a single event (Ruttenberg 1975). In contrast, during RICO, which occurred in early winter, the three most disturbed days had daily rainfall rates between 17 and 22 mm day^{-1} (Snodgrass et al. 2009) and were characterized by moderate convection similar to the code 3 classification from GATE (Garstang and Aspliden 1974; Ruttenberg 1975; Ackerman and Cox 1981; see Table 1). As noted by several RICO publications (e.g., Zhao and Di Girolamo 2007; Knight et al. 2008; Nuijens et al. 2009; Snodgrass et al. 2009, Arthur et al. 2010; Reiche and Lasher-Trapp 2010; Minor et al. 2011) the wintertime trades frequently support convective clouds that precipitate and exhibit a range of cloud-top heights extending up to and above the freezing level (~4.5 km). This disturbed state of the wintertime trades, observed during many days of the RICO experiment, represents an important aspect of the trade wind environment that has not been well investigated.

This paper is the first in a series that focuses on the variability of TMBL properties, particularly water vapor, rather than the mean state of the undisturbed TMBL. The purpose of this paper is to investigate the statistical thermodynamic, moisture, and kinematic properties of the TMBL over the western tropical North Atlantic during RICO. We use the complete set of island-launched soundings from RICO to investigate the statistical characteristics of the TMBL environment for the undisturbed state used as a basis for trade wind cloud simulations by the Global Energy and Water Cycle Experiment (GEWEX) Cloud System Studies (GCSS) investigators (vanZanten et al. 2011), for the disturbed state, which is not included in most modeling investigations, and for all conditions, regardless of state. In doing so, we address questions regarding the use of averaged soundings to characterize the tropical trade wind regime.

In subsequent papers (Davison et al. 2013a,b, hereafter Part II and Part III, respectively), we investigate the spatial structure and time evolution of the water vapor field using soundings and a technique based on layered echoes from S-band radar, which we attribute to Bragg scattering. We demonstrate that thin moisture layers are a persistent, coherent feature of the TMBL that delineate aspects of its mesoscale structure. These papers consider how cloud detrainment, turbulence, and large-scale forcing may contribute to the formation and maintenance of the moisture layering. A statistical analysis of the moisture layers is presented and the behavioral trends of the layers are examined as a function of rain rate and other surface meteorological variables. Based on the statistics in the current paper and the analyses in Part II and Part III, we provide a revised conceptual model of the tropical marine boundary layer for the trade wind environment that incorporates this layering.

TABLE 1. The convective state of the atmosphere as a function of the GATE convective cloud code.

Code	Convective State
1	Extremely depressed convection
2	Slightly depressed convection
3	Weakly enhanced convection
4	Moderately enhanced convection
5	Strongly enhanced convection

2. Data sources and methodology

The data presented in this paper were obtained during the RICO field campaign (Rauber et al. 2007), which was carried out in December 2004 and January 2005. Meteorological conditions during RICO were typical for this region and time of year with only a few weak tropical waves, low- and upper-level troughs, and weak cold fronts affecting the flow and precipitation across the RICO region. Thermodynamic, moisture, environmental, and rainfall characteristics of the RICO region during the field campaign can be found in Snodgrass et al. (2009), Nuijens et al. (2009), and Minor et al. (2011).

The data presented in this paper consist of Vaisala RS92 rawinsondes launched from Barbuda (Fig. 2) at either Spanish Point or the S-Pol radar site from the entire RICO campaign. Two to six rawinsondes were launched daily depending on flight operations. The RS92 provides improved humidity measurements over previous versions because of prelaunch reconditioning and a heated twin-sensor design (Währn et al. 2004). The total uncertainty in sounding relative humidity (RH) measurements was 5%, the repeatability in calibration was 2%, and the reproducibility was 2% (Vaisala 2010).

FIG. 2. Map of the northwestern Caribbean islands. Rawinsondes were launched from either the S-Pol site (A) on the southwestern side or Spanish Point (B) on the southeastern side of Barbuda. Map courtesy of Google Maps.

Measurements were recorded at 1 Hz (~5-m interval). The final RICO quality controlled sounding dataset consists of 141 rawinsondes.

To conduct the analysis on a standard grid while retaining the full extent of the environmental variability measured by the rawinsondes, the data were linearly interpolated to 1 m. Soundings that traversed clouds were included in these analyses. The rawinsonde data are presented using essentially the same approach as the contoured frequency by altitude diagrams utilized by Yuter and Houze (1995), although the diagrams provided herein use actual bin values rather than contours [referred to as frequency by altitude diagrams (FADs)]. This allows full characterization of the variability and modal characteristics of the environmental profiles.

In keeping with the analysis of Zhao and Di Girolamo (2007), which will be utilized in Part III, vertical bins of 100-m depth were used in generating the FADs, with the data being normalized for each altitude bin. In some figures, we reduced the vertical bin to 25 m to illustrate specific points. Fundamental meteorological variables as well as their vertical gradients were examined. Vertical gradient calculations for a given variable were made by direct subtraction (higher-altitude value minus lower-altitude value) for two different height intervals (Δz = 50 and 350 m). The value of the gradient was assigned at the altitude corresponding to the midpoint of the gradient interval. The two gradient intervals were chosen to roughly reflect sublayer and cross-layer variability, respectively, and correspond to radar analyses of moisture layers presented in Part II and Part III.

Data were grouped into five categories: 1) all soundings (ALL); 2) soundings from the suppressed period chosen by the GCSS working group, 16 December 2004–8 January 2005 (GCSS; vanZanten et al. 2011); 3) soundings excluded from this GCSS period (A–G); 4) suppressed soundings (SUP), as determined by rain rates less than 1.75 mm day^{-1} from Snodgrass et al. (2009); and 5) active soundings (ACT), as determined by rain rates greater than 1.75 mm day^{-1} from Snodgrass et al. (2009).[1] The GCSS and SUP soundings will jointly be referred to as undisturbed and the A–G and ACT soundings as disturbed. Table 2 summarizes the number of soundings and days in each category.

3. Results

a. Relative humidity

Figure 3a, which is a FAD of RH from the surface to 8.0 km for ALL, shows that the RH field is highly variable both within and above the TMBL. At 2.0 km, half of the observed RH values fall within the range 56%–89%, while at 4.0 km, half are within 13%–61% (Fig. 3a). There were no obvious peaks in the distributions between these two elevations. Along the main "ridge" connecting the modes in the frequency distributions, half of the RH values fall within a range of about 8% below the top of the mixed layer. The median within the surface-based mixed layer increases from about 77% at

[1] Snodgrass et al. (2009) rain-rate figure used to determine SUP and ACT categories is shown in Part III (Fig. 10). Actual break used was between 16 Jan 2005 (1.85 mm day^{-1}) and 15 Jan 2005 (1.62 mm day^{-1}). No soundings were taken on days prior to 7 Dec 2004.

TABLE 2. Number of soundings and days for sounding classifications.

	All	GCSS	A–G	SUP	ACT
No. of soundings	141	55	86	84	57
No. of days	49	24	25	30	19

the surface to about 89% at 0.5 km. At 0.5 km, half of the RH values were between 84% and 93%, with extreme values in bins centered on 69% and 99%. From the mixed-layer top to 2.0 km, the spread widens, such that half the values are found within a range of about 10% RH at 1.0 km and 33% RH at 2.0 km. Above the mixed layer, the median decreases in a stepped pattern to about 7% at the top of the diagram. Above 4.0 km, a ridge in the distribution appears below 15% RH, sharpening above 5.0-km elevation. A particularly important feature of this figure, as well as Figs. 3b–e and 4, is the large variability found in RH.

Figures 3b and 3d show the FADs for the GCSS and SUP undisturbed periods. Figures 3c and 3e show the corresponding FADs for the A–G and ACT disturbed periods. To compare the categorizations for the undisturbed (disturbed) periods, the GCSS (A–G) median is plotted in red on the SUP (ACT) FAD. Figures 4a–d shows the GCSS, A–G, SUP, and ACT FADs, but with 25-m

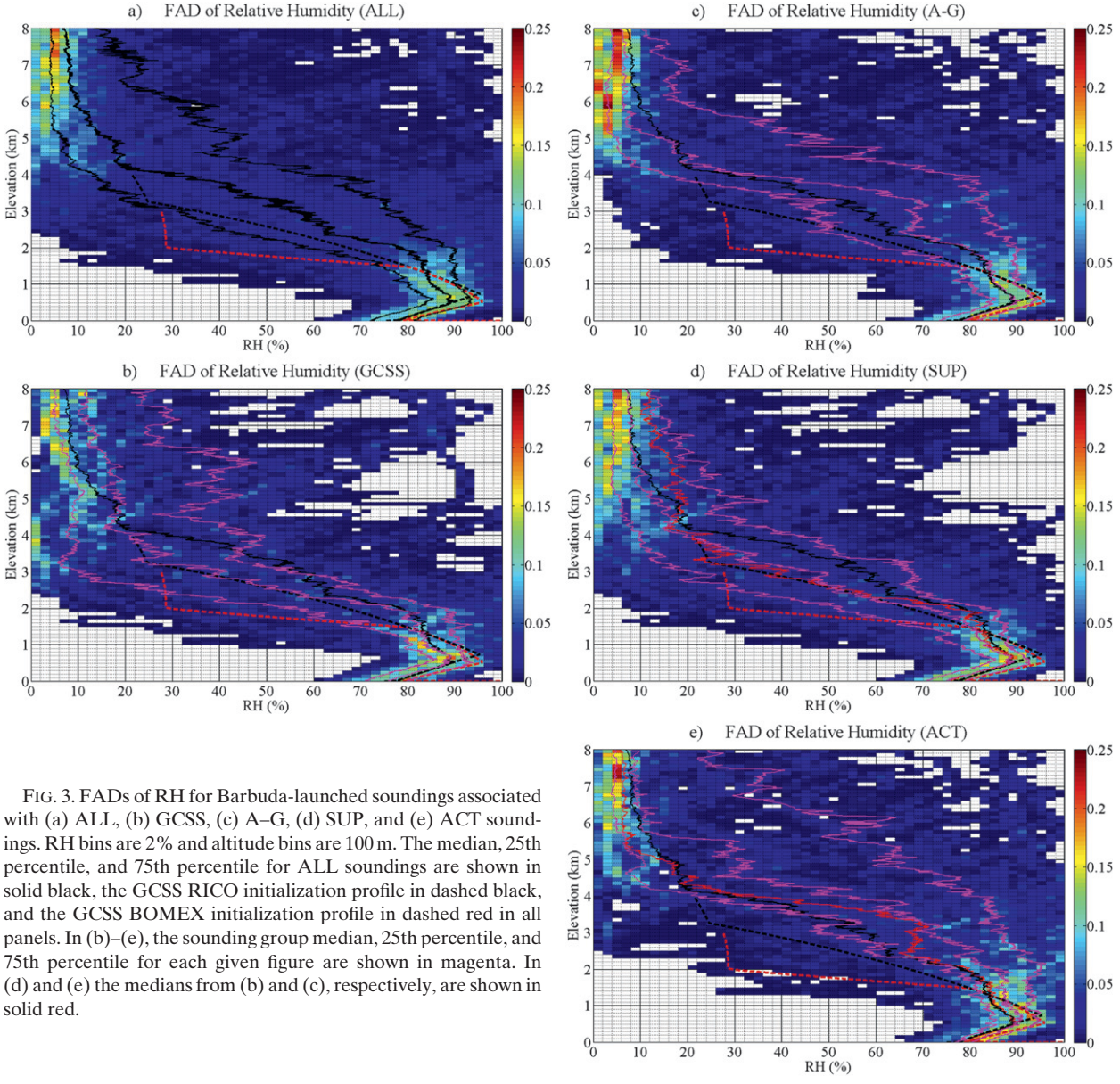

FIG. 3. FADs of RH for Barbuda-launched soundings associated with (a) ALL, (b) GCSS, (c) A–G, (d) SUP, and (e) ACT soundings. RH bins are 2% and altitude bins are 100 m. The median, 25th percentile, and 75th percentile for ALL soundings are shown in solid black, the GCSS RICO initialization profile in dashed black, and the GCSS BOMEX initialization profile in dashed red in all panels. In (b)–(e), the sounding group median, 25th percentile, and 75th percentile for each given figure are shown in magenta. In (d) and (e) the medians from (b) and (c), respectively, are shown in solid red.

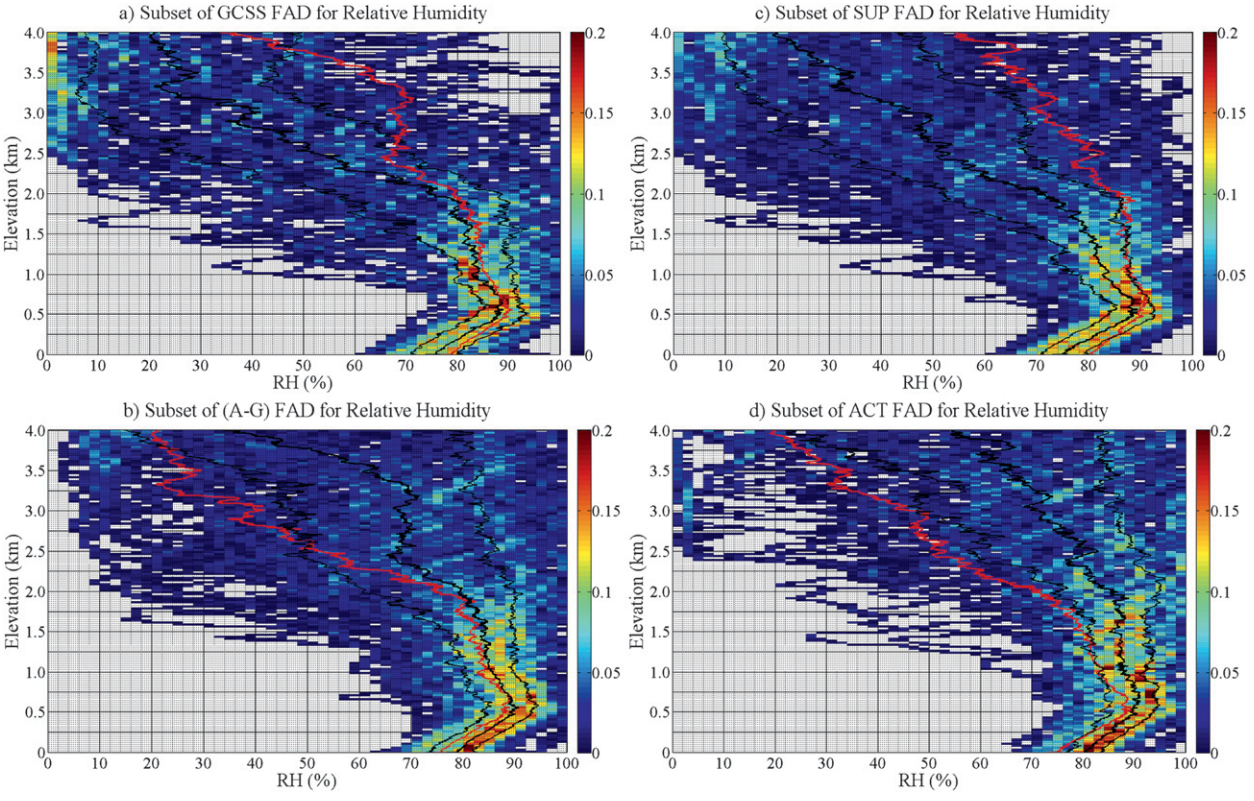

FIG. 4. FADs of RH for Barbuda-launched soundings associated with (a) GCSS, (b) A–G, (c) SUP, and (d) ACT soundings. RH bins are 2% and altitude bins are 25 m. The sounding group median, 25th percentile, and 75th percentile for each given figure are shown in black. In (a)–(d), the median for A–G, GCSS, ACT, or SUP, respectively, is plotted in red.

vertical bins between the surface and 4.0 km. To better compare the character of the disturbed and undisturbed periods, the median for A–G (ACT) is plotted in red on the GCSS (SUP) FAD and vice versa in Fig. 4.

There is an appreciable difference between the disturbed and undisturbed categories for the GCSS subcategorizations (GCSS and A–G) and the subcategories based on the Snodgrass et al. (2009) daily rain rates (SUP and ACT). In Figs. 4a and 4b, the GCSS and A–G medians show little difference below 2.0 km, closely tracking the ALL median (Figs. 3b,c). Above 2.0 km, the GCSS and A–G medians diverge to a maximum difference of about 50% RH just above 3.0 km, and then converge back to the ALL median at 4.0 km. Above 5.0 km the GCSS and A–G medians deviate away from the ALL median, with the GCSS showing moister conditions than does the A–G sounding subset.

In contrast, the difference between the ACT and SUP medians is more substantial. At the surface, the median RH for ACT is about 5% greater than for SUP. This difference decreases to about 1% at the mixed-layer top but then increases such that above 750 m, the SUP median lies along or to the left of the 25th percentile line on the ACT FAD and the ACT median lies along or to the right of the 75th percentile line on the SUP FAD. The ACT median shows moister conditions than SUP from the surface to 8.0 km, with maximum differences of 30%–40% RH between 3.0 and 4.0 km.

These data suggest that segregating soundings by daily rain rate is a better approach to distinguishing disturbed from undisturbed conditions when generating model initialization profiles. Note also that both the RICO and BOMEX model initialization profiles in Fig. 3 lie to the right of the ridges in the frequency distributions for all five categories between the mixed layer top and 1.3 km, suggesting that the models are being initialized with deeper mixed layers and higher RH values in the lower TMBL than occur on the majority of soundings. However, between 1.3 and 2.4 km, the RICO initialization profile has RH values 5%–10% lower than the GCSS median, although the values closely follow the SUP median.

The FAD of ALL vertical RH gradients ($\Delta z = 350$ m) shown in Fig. 5 exhibits several noteworthy characteristics. A large range of ΔRH values was observed. This range was bounded by extreme RH decreases of nearly 100% $(350\,\text{m})^{-1}$ and increases of more than 60% $(350\,\text{m})^{-1}$, with measured values in nearly every bin in

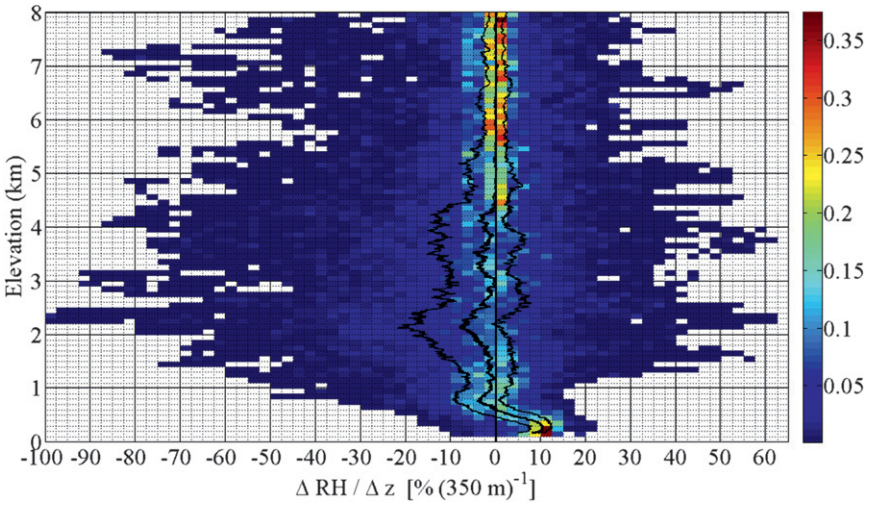

FIG. 5. FAD of ΔRH for $\Delta z = 350$ m. Bins for ΔRH are 2.5% and altitude bins are 100 m. Values of ΔRH were assigned at the midpoint of each 350-m interval. The median, 25th percentile, and 75th percentile are shown in black.

between. Although the RH median decreases with height above the mixed layer, both positive and negative vertical RH gradients were routinely present on individual soundings. The ridge in the distribution near ΔRH = 0% is relatively sharp above 4.0 km but is fairly flat between 4.0 km and the top of the mixed layer.

b. Temperature

The distribution of temperature T for ALL soundings was about 6 K wide at the mixed-layer top (~0.5 km) and 8–9 K wide between 2.0 and 8.0 km (see Fig. 6). Within the mixed layer, half the temperature values were within 1 K at any given altitude. At 2.0 km, half the values were within 2 K. Below 2.4 km, there was little difference between the medians for all five categories (subcategories not shown). Between 2.4 and 4.7 km, the GCSS and SUP medians exceed the A–G and ACT medians by a maximum of about 1 K near 3.6 km. Above 4.7 km, little difference again exists in the medians of the five categories. The character of the distributions below 1.5 km was quite similar. However, between 1.5 and 2.5 km, the ridges in the GCSS and SUP distributions were flat while the A–G and ACT distribution ridges were sharp, implying that narrower ranges of temperatures were common at these altitudes during the disturbed cases. Between 2.5 and 4.0 km, the A–G and

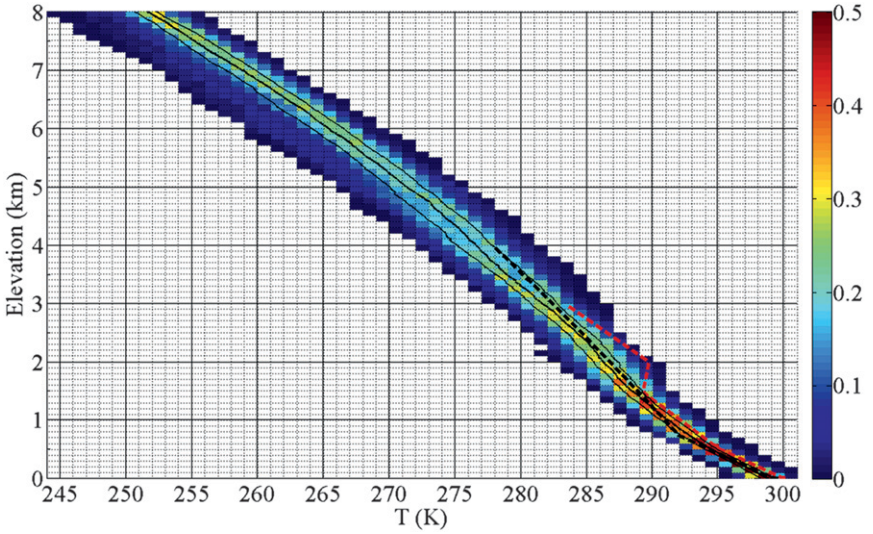

FIG. 6. FAD of T, with 1-K bins. See Fig. 3a for line conventions.

ACT distribution ridges were about 1–2 K colder than for the GCSS and SUP ridges.

It is commonly thought that the TMBL top is associated with a distinct temperature inversion. For this reason, temperature gradients are of particular interest in this environment. However, as can be seen from both the 50- and 350-m temperature gradients for ALL data (Figs. 7a,b), inversions were found in all altitude bins above 1.2 km for both gradient intervals. There was a very slight preference for inversions to occur between 1.5 and 2.8 km (Fig. 7c). Note also that there are cases where superadiabatic lapse rates were present. These observations of absolute instability will be explored in section 3h.

c. Specific humidity

Like the RH FAD, the specific humidity (q) FAD for ALL data shows wide ranges in observed values for given altitude bins. The values between the 25th and 75th percentile lines range over 1.8, 3.1, and 3.9 g kg^{-1} at 1.0, 2.0, and 3.0 km, respectively. The maximum range in q, nearly 13.5 g kg^{-1}, was centered near 1550 m (Fig. 8a). The vertical trends in q mirror the trends in RH. Specifically, the GCSS and A–G medians closely align with the ALL median below 2.4 km, while the SUP and ACT cases show lower and higher medians, respectively, compared to ALL (Figs. 8b–e). Above 2.4 km, the q medians for A–G and GCSS diverge to a maximum difference of about 4.0 g kg^{-1} just above 3.0 km. The SUP and ACT medians continue to diverge to a maximum difference of about 3.7 g kg^{-1}. In general, direct parallels can be drawn between the RH observations and those observed in q, except that the q trends are more subtle. Figure 9 shows the $\Delta q/\Delta z$ for $\Delta z = 350$ m. Although both the distribution ridge and the median gradients are negative, implying decreases of q with height, many cases were observed where q increased with altitude. In general, layers with $\Delta q/\Delta z > 0$ are most likely to be associated with past cloud detrainment. For example, about 25% of the soundings had $\Delta q/\Delta z > 0$ at elevations above about 2.5 km.

d. Wind direction

Figure 10 shows the FADs for wind direction. For ALL soundings (Fig. 10a), the median surface wind direction was 70°, veering to almost 80° at 1.0 km. Between 1.0 and 4.0 km, the median wind direction gradually backed to 50°. Between 4.0 and 5.0 km, the median wind direction shifted rapidly, through 0°, becoming northwesterly above 5.0 km. If we define the ''trade wind layer'' as the layer with winds from the east-northeast (45°–90°), over half the soundings showed the trade wind layer extending above 4.0 km for all five categorizations. However, below about 4.0 km, both the median wind directions and the ridges in the distributions for the disturbed categories (A–G and ACT) were about 10°–20° more easterly (i.e., less northerly) than both undisturbed classifications (GCSS and SUP), implying that, on average, disturbed conditions were associated with TMBL air originating from more tropical latitudes. Above 4.0-km altitude, the directional shift in the medians associated with the top of the (wind defined) trade wind layer occurred more sharply for the disturbed categories than for the undisturbed, indicating that the layer of easterlies was deeper for the undisturbed categories. The wind direction medians for the disturbed categories reached 0° below 4.5 km while the undisturbed medians reached 0° above 5.0 km. For the GCSS soundings, very few cases occurred where the winds had a westerly component below 4.0 km.

e. Wind speed

The wind speed FAD for ALL data is shown in Fig. 11. The median wind speed increases slightly from just below to just above 10 m s^{-1} through the mixed and transition layers (0.1–0.8 km) (Fig. 11). Between 0.8 and 2.8 km there is an almost linear decrease of the median wind speed with height. Between 2.8 and 5.2 km, the median wind speed is nearly constant at about 6 m s^{-1}, generally increasing with height above 5.2 km. The range of wind speeds below 5.0 km extended from 0 to about 17 m s^{-1}, with the majority of the observations below 5.0 km within 4 m s^{-1} of the median value. There were no major differences between the various categorizations.

f. Potential temperature

Figures 12a–d show potential temperature (θ) FADs for the GCSS, A–G, SUP, and ACT categories, respectively. First, comparing GCSS with A–G, a well-defined mixed layer appears in the GCSS FAD, with a top near 0.5 km. The mixed layer is present, but less well defined in the A–G FAD. The A–G median is about 0.5 K warmer than the GCSS median at 1.0 km, but about 1.6 K colder at 3.5 km, implying less stable conditions for the A–G soundings. The crossover of the medians occurs between 2.0 and 2.5 km. Comparing SUP and ACT, we see a well-defined mixed layer with a top near 0.5 km for the SUP soundings, but for the ACT soundings, the mixed layer is poorly defined. The ACT and SUP medians are near coincident between 0.75 and 1.5 km. Between 1.5 and 4.0 km, the median θ for ACT becomes increasingly colder than for SUP, implying less stable conditions, consistent with the greater daily rain rates. The difference between the medians (SUP minus ACT) was 0.6 K at 2.5 km and 1.1 K at 3.5 km.

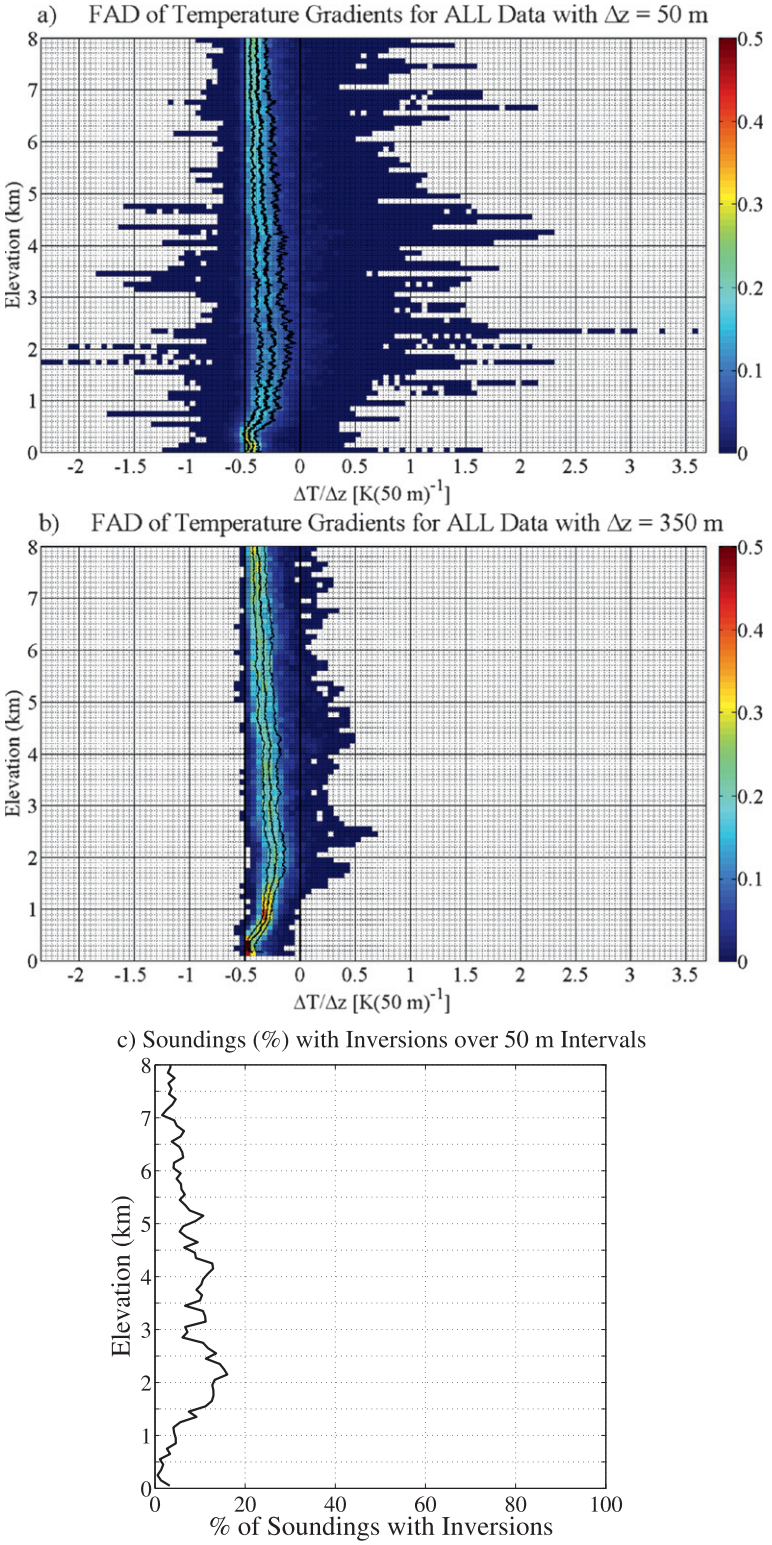

FIG. 7. FADs of ΔT for Δz = (a) 50 and (b) 350 m. Both have 0.05-K bins and units are matched to Δz = 50-m interval for easy comparison. Both the dry adiabatic lapse rate and isothermal curve are plotted in addition to the figure median, 25th percentile, and 75th percentile, all in black. (c) Percentage of soundings having inversions across 50 m in each 100-m vertical bin [calculated from (a)].

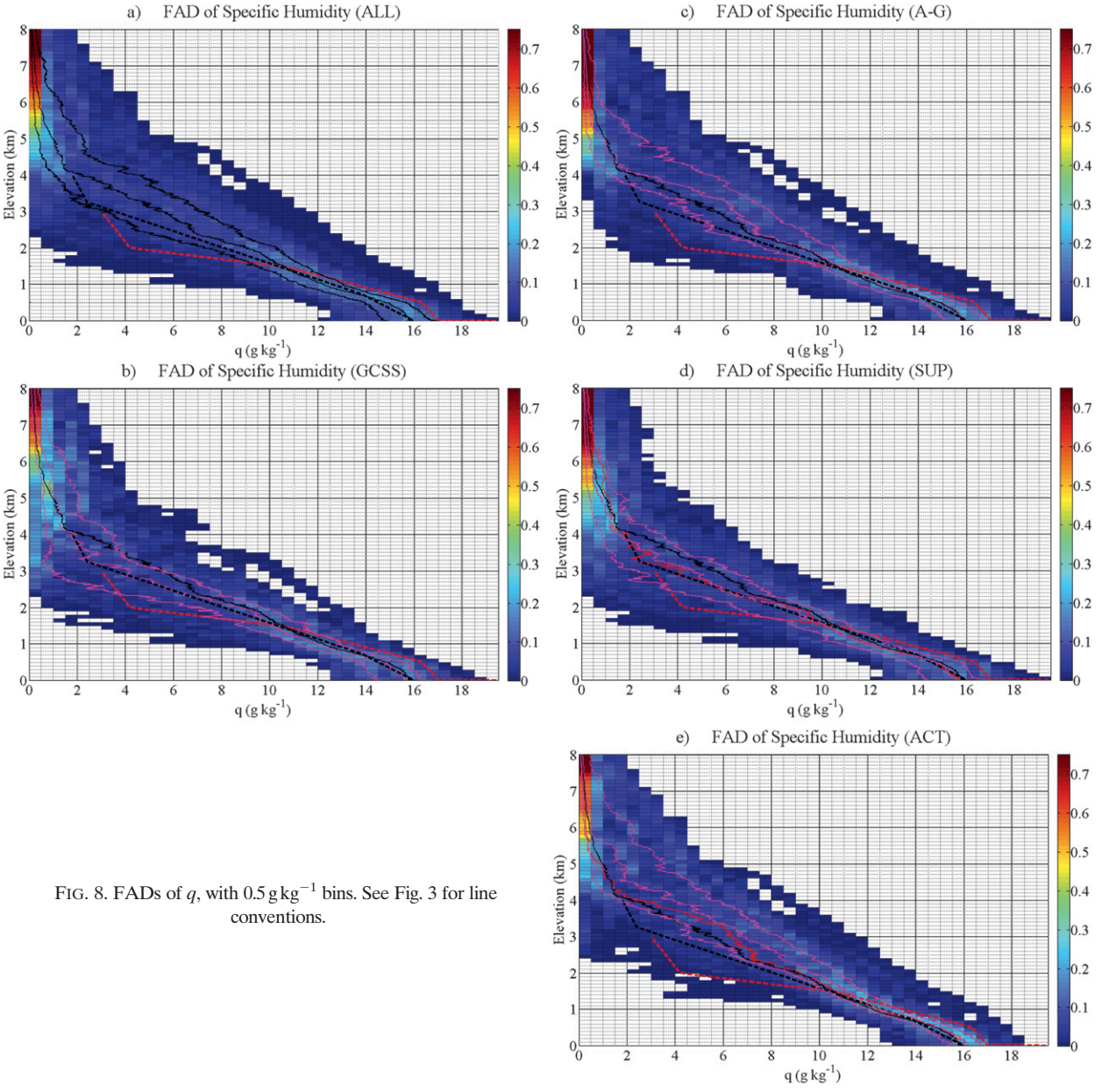

FIG. 8. FADs of q, with 0.5 g kg^{-1} bins. See Fig. 3 for line conventions.

g. *Equivalent potential temperature*

The equivalent potential temperature θ_e was calculated following Fierro et al. (2009), who used the Emanuel (1994) formulation and calculated the lifting condensation level using an iterative procedure. The distribution of θ_e for the ALL FAD is very wide (see Fig. 13a). Throughout the mixed and transition layers (from the surface to 0.8 km) the range of θ_e values for a given altitude is on the order of 15 K, with half the values within a range of 5 K. The range of θ_e values for the altitudes between 0.8 and 5.0 km increases to a maximum of about 35 K near 2.5-km altitude, with half of the values within a range of about 12 K. This large spread in the midlevel θ_e values reflects both the influence of moistening from the ocean as well as the dry air from above the TMBL. Visually, one can trace the (positively sloped) higher-altitude distribution ridge downward to account for the lowest θ_e values near 2.0 km. The influence of the oceanic moisture influx can be seen throughout the warmer (more upright, but negatively sloped) θ_e values on the right side of the distribution.

Figures 13b and 13d show the θ_e FADs for the GCSS and SUP undisturbed periods to an altitude of 8.0 km.

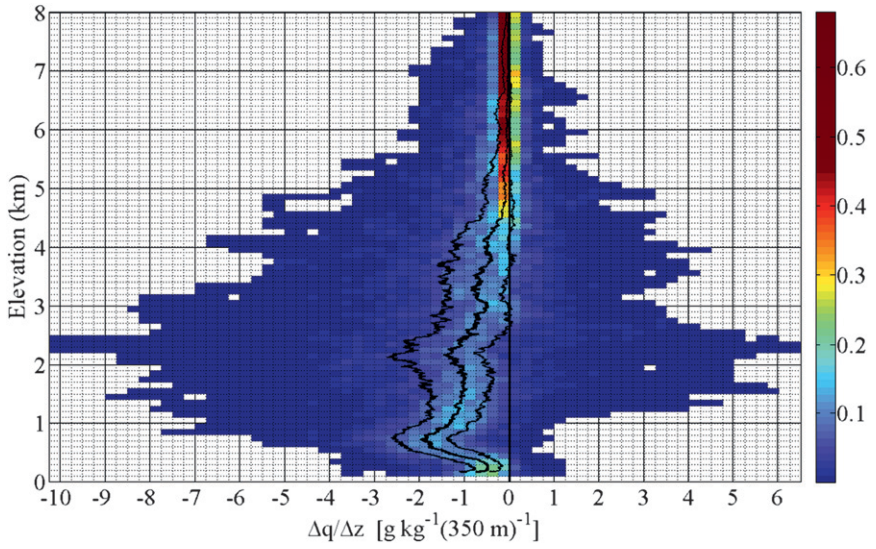

FIG. 9. FAD of Δq for $\Delta z = 350$ m, with 0.25 g kg^{-1} bins. The figure median, 25th percentile, and 75th percentile are shown in black.

Figures 13c and 13e show the corresponding FADs for the A–G and ACT disturbed periods. Figures 14a–d show the GCSS, A–G, SUP, and ACT FADs, but with 25-m vertical bins between the surface and 4.0 km. In Fig. 14, the median for A–G (ACT) is plotted in red on the GCSS (SUP) FAD and vice versa to better compare the character of the disturbed and undisturbed periods.

Throughout the lowest 4.0 km, the GCSS median θ_e was lower than the A–G median θ_e. The same was true for the SUP and ACT θ_e medians. The spread in the medians [(A–G) minus GCSS] ranged from 1.0 to 3.0 K between 0.5 and 2.5 km, while the spread in the medians (ACT minus SUP) ranged from 0.7 to 6.2 K. At 3.0 and 3.5 km, both spreads approach about 5–6 K. At and above 4.0 km, the A–G and GCSS medians are nearly coincident with the ALL median, while the ACT-minus-SUP spread continues to nearly 8.0 km. The different behavior of the medians reflects the trends in moisture evident in the RH and q FADS (Figs. 3, 4, and 8).

Both disturbed classifications had more peaked distributions than those associated with the undisturbed categorizations below 1.5 km. At altitudes between 2.5 and 4.0 km, a bimodal distribution of θ_e was present. For example, at 3.0 km on the GCSS and SUP FADs, a mode associated with the dry air aloft is present near 313 K and a second mode associated with moist oceanic air is present near 326 K. Between 2.0- and 4.0-km altitudes, the ranges for the A–G and ACT distributions extend to higher θ_e values, most likely showing the effects of convective moisture transport. The supposition that this is a moisture effect is supported by comparison with the θ medians. The GCSS and SUP medians have higher θ values compared to the A–G and ACT medians, opposite of what would be expected if it was a temperature effect.

If one defines the tropical marine boundary layer as the part of the atmosphere that is significantly influenced by the ocean's moisture, then, based on the median behavior (the elbow in the median lines), the θ_e median would indicate that the top of the TMBL is about 4.0 km for ALL soundings (Fig. 13a). Using this definition, the TMBL top altitude varies with sounding classification, tending to extend higher on disturbed days than on undisturbed. The TMBL median top was at about 4.3 km for the ACT cases, about 4.0 km for the A–G cases, about 3.6 km for the SUP cases, and about 3.3 km for the GCSS cases. For the disturbed cases, the median TMBL top is near the altitudes where the wind direction shifts from northeasterly to northwesterly. For the undisturbed cases, these two levels appear to be unrelated.

h. Virtual potential temperature

Figures 15a and 15b show the virtual potential temperature (θ_v) and θ_v gradient ($\Delta z = 50$ m) FADs, respectively, for ALL data. The mixed layer has a strong ridge in the distribution corresponding to the dry adiabatic lapse rate. Between 0.5 and 1.4 km, the median lapse rate stabilizes, approaching the moist adiabatic lapse rate. Half the values were within a range of 2.0 K at 2.0 km and 2.6 K at 4.0 km. The largest median vertical θ_v gradients occur between 1.4 and 2.4 km and very gradually decrease with height above this level. Half the values were within about 0.25 K (50 m)$^{-1}$, but the remaining half are spread over a much wider distribution.

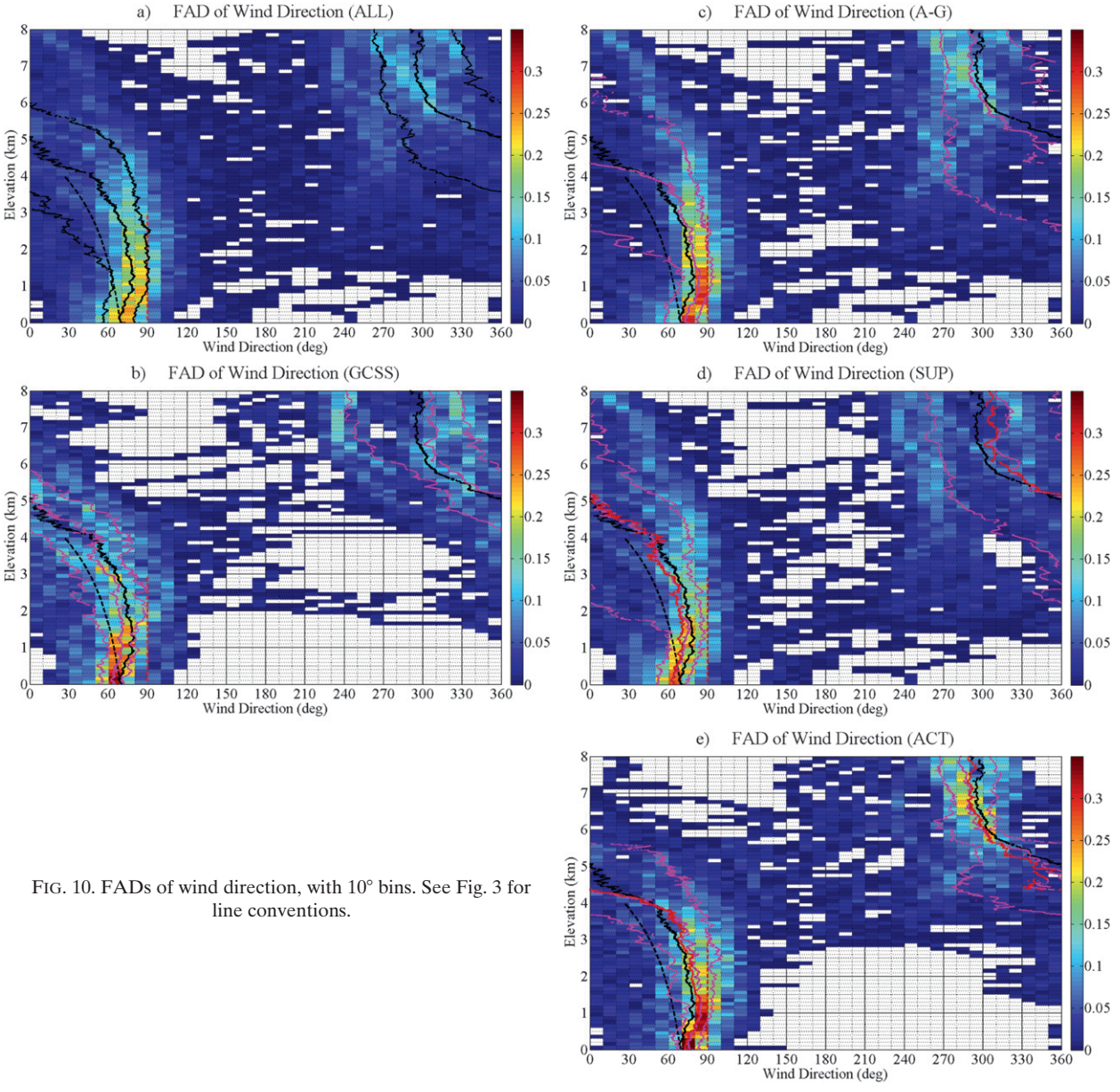

FIG. 10. FADs of wind direction, with 10° bins. See Fig. 3 for line conventions.

The right tails of these distributions appear to have little dependence on height above 1.5 km, indicating that regions of large static stability occur at all altitudes—and thus are not limited to a narrow range of altitudes normally associated with the TMBL top.

Negative gradients of θ_v were observed, the strongest of which were associated with soundings either in or near saturated air. It is likely in these cases that the sondes passed through clouds or closely grazed clouds. Negative gradients were observed in some cases when the sonde appeared to enter cloud. In other cases, the negative gradients were observed when the sonde appeared to exit cloud (Fig. 16). Many of the largest negative gradients of θ_v were observed when the cloudy air was colder than the air below it (e.g., Figs. 16a,b). The portions of the clouds being sampled may have been evaporating. In these instances, instrument wetting and subsequent evaporative cooling cannot explain the negative θ_v gradients because the sonde is entering the cloud when the negative gradient is observed, not exiting it. Negative θ_v gradients also occurred when the air above the cloud was colder than the cloudy air. In these instances, instrument wetting and subsequent evaporative cooling could be considered a valid explanation for the negative gradients.

We consulted sounding experts at NCAR (J. Wang and T. Hock 2012, personal communication), who

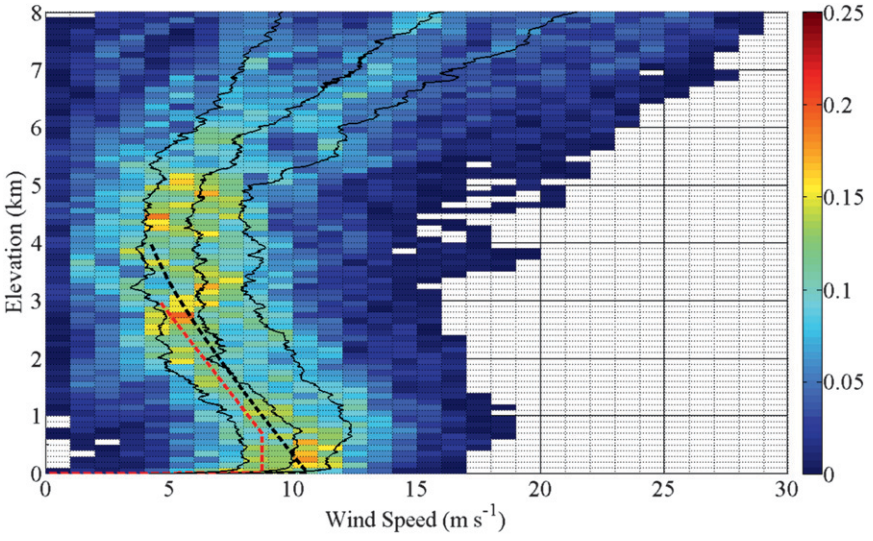

FIG. 11. FAD of wind speed, with 1 m s^{-1} bins. See Fig. 3a for line conventions.

expressed the opinion that many of the largest negative θ_v gradients for soundings where the cloudy air was warmer than the air above it represented true environmental instability (e.g., Figs. 16c,d), although cases with sensor wetting and evaporative cooling did exist. The key discriminator they identified is the nature of the spikes (decrease and rebound) in both θ_v and RH, given that they are measured by different instruments on the sounding package. Only the temperature sensor responds to evaporative cooling. When correlated spikes

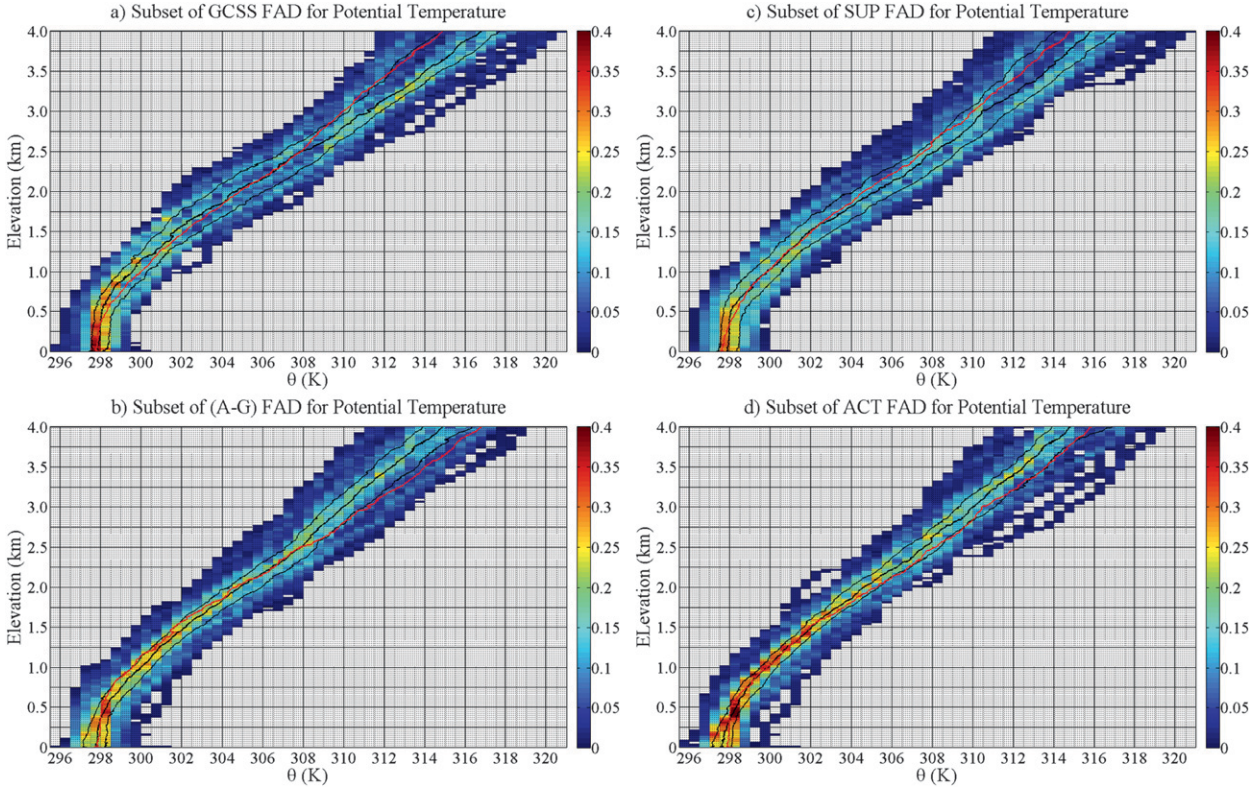

FIG. 12. FADs of θ, with 0.5-K bins. See Fig. 4 for line conventions.

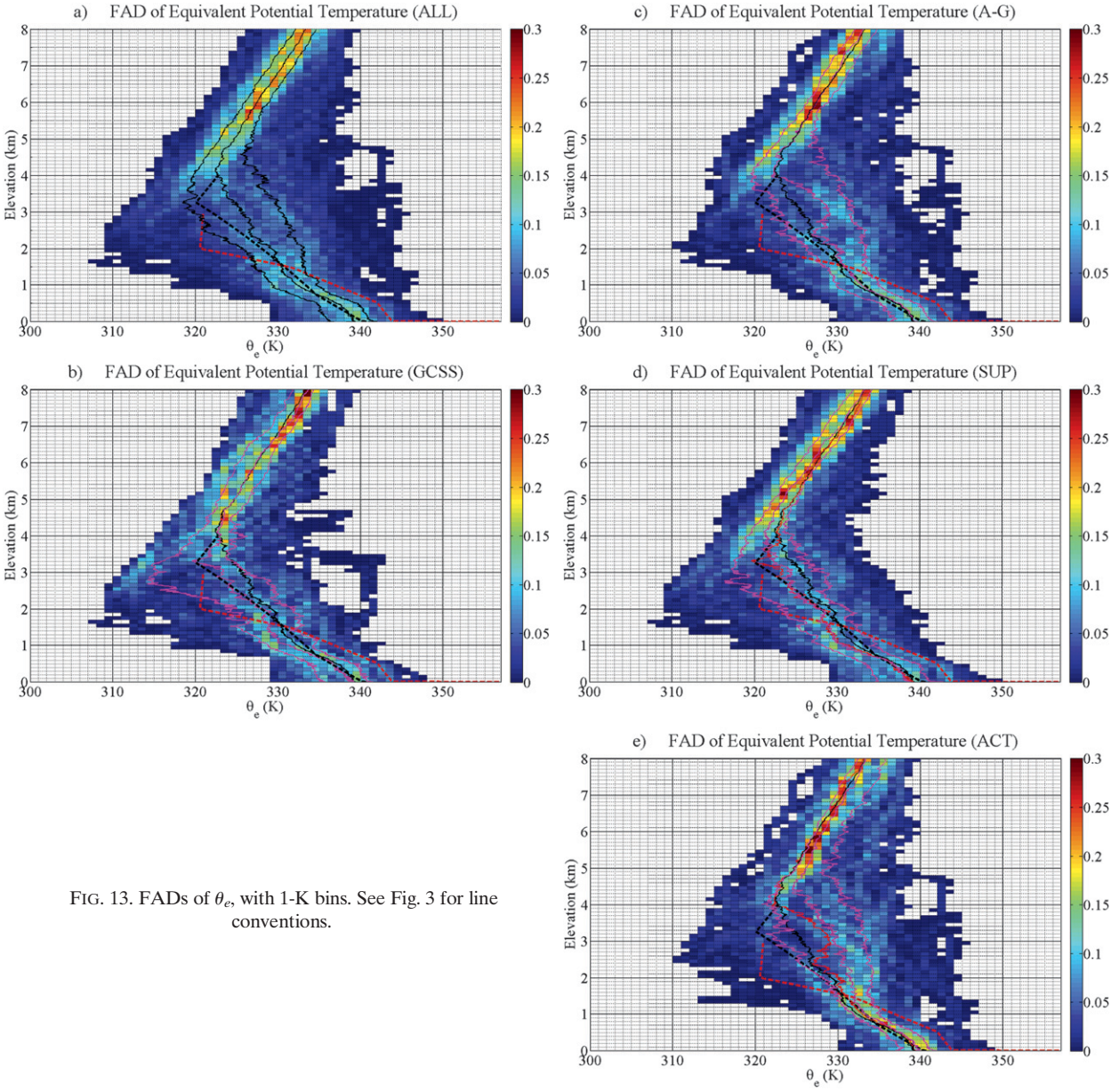

FIG. 13. FADs of θ_e, with 1-K bins. See Fig. 3 for line conventions.

occur in both variables at the same altitudes, the measurements most likely reflect true instability. When θ_v rebounds, but RH does not, cooling upon exiting cloud is most likely attributable to evaporative cooling of the wetted sensor. Thus, based on these interpretations, layers of true absolute instability appeared to exist near cloud boundaries.

i. Bulk Richardson number

The gradient Richardson number, derived from theory, determines whether atmospheric flow is turbulent or laminar. The gradient Richardson number must drop below $R = 0.25$ in order for laminar flow to become turbulent, or must climb above $R = 1.00$ for turbulent flow to become laminar. In practice, the Bulk Richardson number R_B is calculated from soundings to estimate the likelihood that airflow will be turbulent and is given by

$$R_B = \frac{g\Delta\theta_v \Delta z}{\overline{\theta}_v[(\Delta\overline{U})^2 + (\Delta\overline{V})^2]},$$

where g is the gravitational acceleration, $\Delta\theta_v$ is the virtual potential temperature change over the vertical distance Δz, $\overline{\theta}_v$ is the average virtual potential temperature, and $\Delta\overline{U}$ and $\Delta\overline{V}$ are the mean vertical shears of the eastward and northward wind components, respectively.

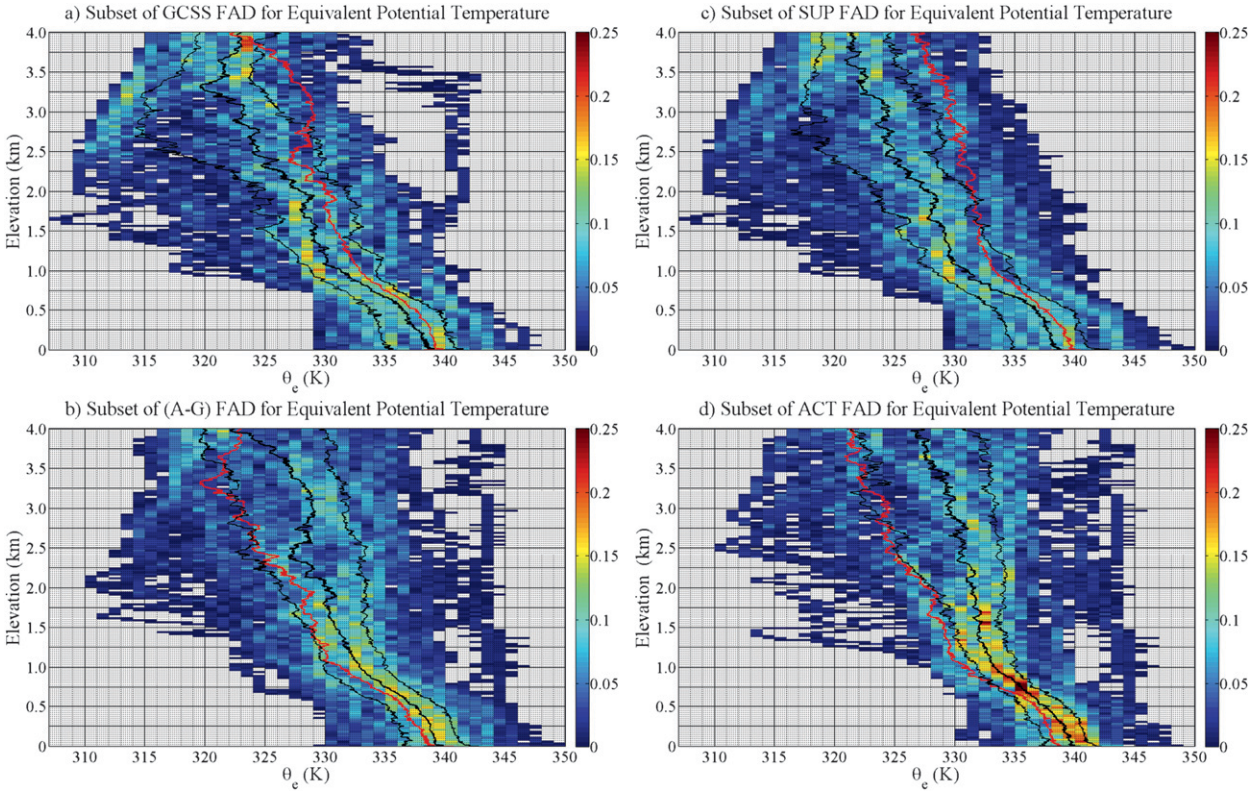

FIG. 14. FADs of θ_e, with 1-K bins. See Fig. 4 for line conventions.

Because of the relative coarseness of the vertical gradients used in R_B calculations, the critical values for R_B will exceed those for the gradient Richardson number, with values dependent on the vertical gradient resolution (e.g., Stull 1988). A FAD of R_B is shown in Fig. 17. Over 25% of the measurements had $R_B < 1.0$. Although the distributions of R_B are wide, the ridge between $R_B = 0.0$ and $R_B = 1.0$ for $\Delta z = 50$ m clearly indicate that the turbulence necessary for Bragg scattering may regularly be present in this environment. This fact will become important in Part II and Part III.

4. Discussion and conclusions

In this paper we examined the variability of TMBL properties, particularly water vapor, over the western tropical North Atlantic during RICO. We used the complete set of island-launched soundings from RICO to investigate the statistical characteristics of the TMBL environment using frequency by altitude diagrams (FADs). The data were also divided into undisturbed and disturbed classifications using two different methods. In the first method, the undisturbed classification included all soundings used to construct the mean RICO sounding, which has served as a basis for initialization of trade wind cloud simulations by GCSS investigators (vanZanten et al. 2011). The disturbed classification included all remaining soundings. In the second method, the undisturbed classification consisted of soundings on all days with a daily average rain rate less than 1.75 mm day^{-1} based on the analysis of Snodgrass et al. (2009). The disturbed classification consisted of all soundings from days with daily average rain rates greater than 1.75 mm day^{-1}. The following conclusions can be drawn from the analyses.

Regarding humidity:

1) The dominant feature of the TMBL was moisture variability. A very wide range of RH values was observed at all altitudes. For example, at 2.0 km, half of the observed RH values fell within the range 56%–89%, while at 4.0 km, half were within 13%–61% for the ALL FAD. There were no obvious peaks in the distributions between these two elevations. The moisture variability shown in these soundings was also present in the RICO flight data and dropsonde data (e.g., Fig. 1; Stevens 2006; see also Part II). The large variability in the RH FADs implies that the mean sounding used for GCSS simulation initializations rarely characterizes the true state of the tropical marine boundary layer, even under undisturbed conditions.

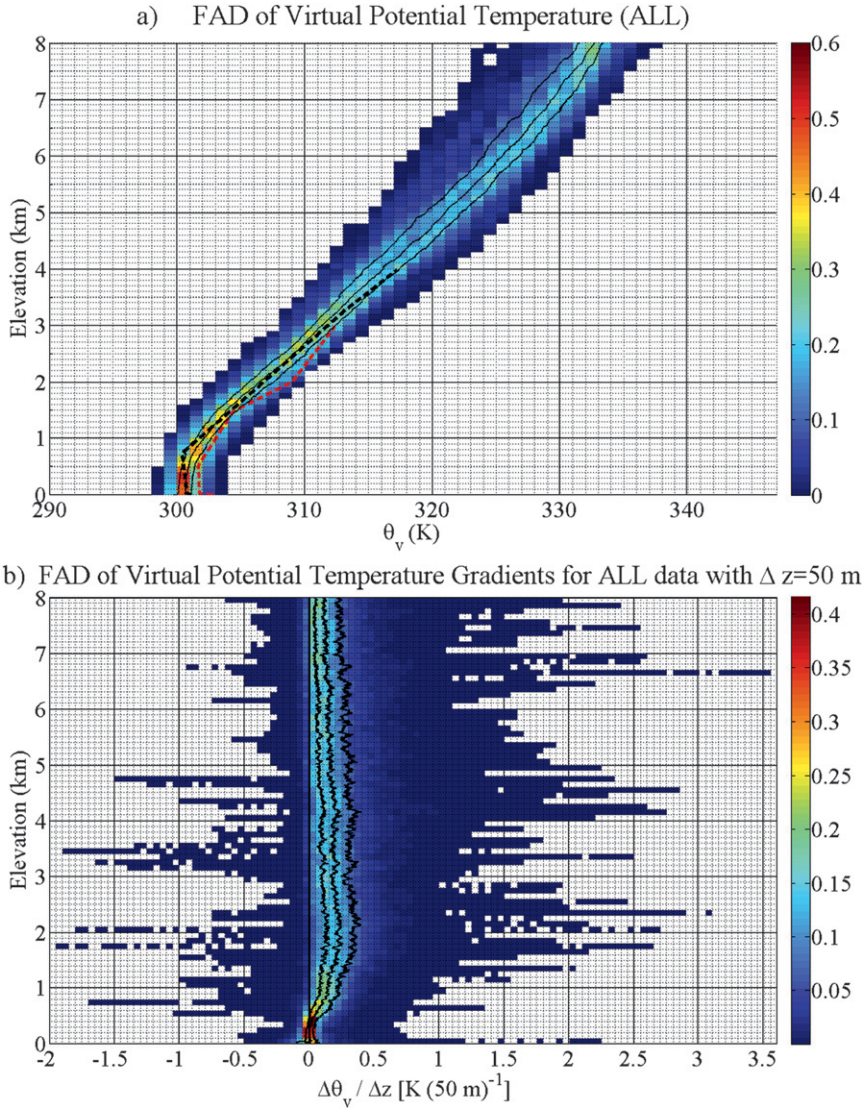

FIG. 15. (a) FAD of θ_v, with 1-K bins. See Fig. 3a for line conventions. (b) FAD of $\Delta\theta_v$ for $\Delta z = 50$ m, with 0.05-K bins. The neutral buoyancy curve, figure median, 25th percentile, and 75th percentile are shown in black.

2) The GCSS and rain-rate methods of separating disturbed from undisturbed conditions yielded different results. Below 2.0 km, the GCSS and A–G medians were nearly identical, while the SUP and ACT medians diverged to a difference of about 15% RH at 2.0 km, with moister conditions for the disturbed category. The greatest differences in RH medians between disturbed and undisturbed conditions occurred between 2.0 and 4.0 km for both methods. Overall, the analyses suggest that the rain-rate method better isolated undisturbed conditions.
3) Considering the rain-rate method, the difference between the ACT and SUP distributions was substantial. For example, above 750 m, the SUP median appeared along or to the left of the 25th percentile line on the ACT FAD and the ACT median appeared along or to the right of the 75th percentile line on the SUP FAD. The ACT median showed moister conditions than SUP from the surface to 8.0 km, with maximum differences of 30%–40% RH.
4) The largest differences in the RH medians between disturbed and undisturbed conditions for both categorizations were found between 3.0 and 4.0 km. Differences in the medians were as large as 50%, with moister conditions observed during disturbed cases.

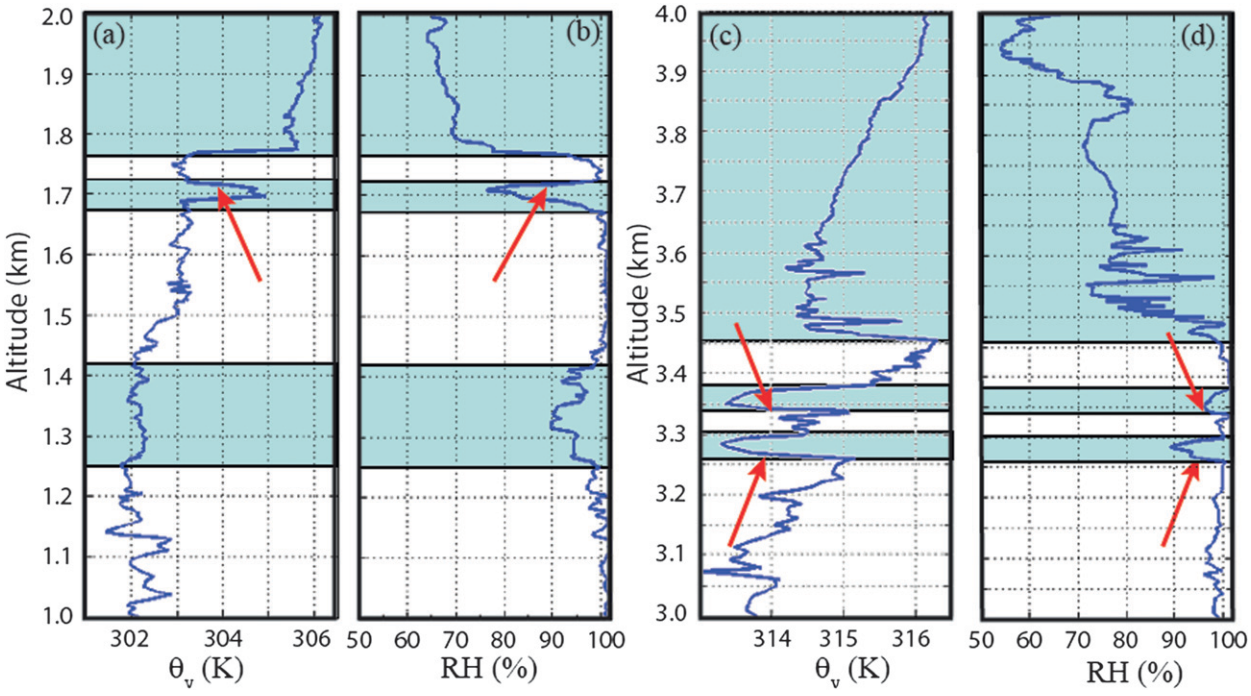

FIG. 16. Profiles of (a),(c) θ_v and (b),(d) RH from two different soundings. The 2358:45 UTC 31 Dec 2004 sounding shown in (a) and (b) has a very unstable layer around 1700 m, which corresponds to the outside environment (blue shading) being almost 2 K warmer than the in-cloud (white shading) θ_v just above. The 1053:40 UTC 16 Dec 2004 sounding shown in (c) and (d) has multiple unstable layers (e.g., ~3250 and ~3450 m), which correspond to the outside environment being almost 2 K colder than the in-cloud θ_v just below. The altitude cohesion in the θ_v and RH profiles in (c) and (d) suggest that the measurements are real and not a result of instrument wetting.

5) Moist air generally extended higher on disturbed days than on undisturbed days.
6) Very large positive and negative vertical RH gradients [>20% $(350\,\text{m})^{-1}$] were common in the soundings.

Regarding TMBL vertical structure:

1) There were two primary ridges in the θ_e FADs, one representing dry air aloft and the other representing air moistened by the ocean. If one defines the tropical

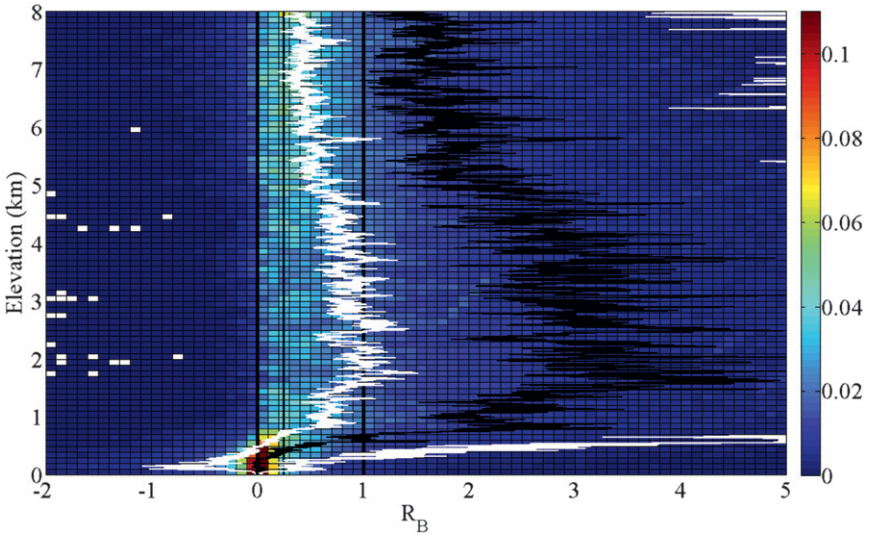

FIG. 17. FAD of R_B for $\Delta z = 50$ m, with 0.1 bins. Critical values of $R_B = 0.0, 0.25$, and 1.0, as well as the figure median, are shown in black. The 25th percentile and 75th percentile are shown in white.

marine boundary layer as the part of the atmosphere that is influenced by the ocean's moisture, then the θ_e FADs would suggest that the top of the boundary layer is about 4.0 km in the RICO environment during the winter season. This altitude is consistent with both the RH and wind direction FADs.

2) There were no dominant heights for temperature inversions and most inversions found were fairly weak. Inversions were observed in every altitude bin above 1.2 km over both 50- and 350-m intervals.
3) The FADs of wind direction indicated that winds within the TMBL originated from more tropical latitudes on days classified as disturbed for both methods of classification.
4) The layer of easterlies typically extended above 4.0 km and generally extended higher on undisturbed days than on disturbed days, with differences in the median vertical extent of the easterlies of more than 0.5 km.
5) On disturbed days, the base of the layer of directional wind shear was coincident with the top of the moist layer (~4.0 km). On undisturbed days, the two parameters were not coincident.
6) The modal ridges and the medians for disturbed days had θ values generally about 1 K colder than for undisturbed days between 2.0 and 4.0 km. This stands in contrast to the observation that the winds on the disturbed days tend to come from more tropical latitudes. One possible explanation is that more evaporative cooling is occurring within this altitude range on disturbed days.
7) The bulk Richardson number FAD suggests that conditions supporting turbulent mixing were often present in the TMBL. This finding is important for interpretation of data in Part II and Part III.
8) Shallow superadiabatic layers were observed on some soundings. Many appeared to be associated with either entering or exiting cloudy air. Only some of these cases could be attributed to instrument wetting.

Although the undisturbed state of the trades has been the focus of nearly all studies that explore the typical state of the trade wind environment, we note that the disturbed state may be equally, if not more, important to the evolution of the trade wind boundary layer, particularly because of deeper vertical mixing and latent heating associated with increased rainfall. Many days during RICO could be considered disturbed. The FADs presented in this paper show distinct differences between these two states.

This work has implications for how we view this environment with respect to modeling. The oversimplified and highly suppressed conditions that often characterize many model simulations of this environment are not often representative of the conditions observed in this environment during RICO. This statement is underscored by the GCSS initialization profiles plotted in the nongradient FADs. Modeling studies that incorporate the layered structure (see Part II and Part III) and high level of moisture variability should be undertaken to ascertain how such variability affects our perception and parameterizations of this environment, especially as they pertain to the radiation, energy, and water budgets of the tropics.

Acknowledgments. We especially thank the NCAR Earth Observing Laboratory RICO scientists and staff for their efforts in the field. Thanks to Junhong Wang and Terry Hock for their insight into identifying instrument wetting/evaporative cooling (and the lack thereof). We also thank Charles Knight, Tammy Weckwerth, and an anonymous reviewer for their constructive comments. Thanks also to the University of Louisville Department of Physics and Astronomy for hosting the lead author during a portion of this work. This research was supported by the National Science Foundation (NSF) under Grants ATM-03-46172 and ATM-08-54954. Additional facilities support at the University of Louisville was provided by DOE Grant DE-SC0005473. Any opinions, findings and conclusions, or recommendations expressed in this publication are those of the authors and do not necessarily reflect the views of NSF or DOE.

REFERENCES

Ackerman, S. A., and S. K. Cox, 1981: Comparison of satellite and all-sky camera estimates of cloud cover during GATE. *J. Appl. Meteor.,* **20,** 581–587.

Arthur, D. K., S. Lasher-Trapp, A. Abdel-Haleem, N. Klosterman, and D. S. Ebert, 2010: A new three-dimensional visualization system for combining aircraft and radar data and its application to RICO observations. *J. Atmos. Oceanic Technol.,* **27,** 811–828.

Berg, L. K., and R. B. Stull, 2005: A simple parameterization coupling the convective daytime boundary layer and fair-weather cumuli. *J. Atmos. Sci.,* **62,** 1976–1988.

Betts, A. K., 1997: Trade cumulus: Observations and modeling. *The Physics and Parameterization of Moist Atmospheric Convection,* R. K. Smith, Ed., Kluwer Academic Publishers, 99–126.

——, and B. A. Albrecht, 1987: Conserved variable analysis of the convective boundary layer thermodynamic structure over the tropical oceans. *J. Atmos. Sci.,* **44,** 83–99.

——, and W. Ridgway, 1988: Coupling of the radiative, convective, and surface fluxes over the equatorial Pacific. *J. Atmos. Sci.,* **45,** 522–536.

Cuijpers, J. W. M., and P. G. Duynkerke, 1993: Large eddy simulation of trade wind cumulus clouds. *J. Atmos. Sci.,* **50,** 3894–3908.

Davison, J. L., R. M. Rauber, and L. Di Girolamo, 2013a: A revised conceptual model of the tropical marine boundary layer. Part II: Detecting relative humidity layers using Bragg scattering from S-band radar. *J. Atmos. Sci.,* **70,** 3025–3046.

——, ——, ——, and M. A. LeMone, 2013b: A revised conceptual model of the tropical marine boundary layer. Part III: Bragg scattering layer statistical properties. *J. Atmos. Sci.,* **70,** 3047–3062.

de Roode, S. R., and C. S. Bretherton, 2003: Mass-flux budgets of shallow cumulus clouds. *J. Atmos. Sci.,* **60,** 137–151.

de Rooy, W. C., and A. P. Siebesma, 2008: A simple parameterization for detrainment in shallow cumulus. *Mon. Wea. Rev.,* **136,** 560–576.

Emanuel, K. A., 1994: *Atmospheric Convection.* Oxford University Press, 580 pp.

Fierro, A. O., J. Simpson, M. A. LeMone, J. M. Straka, B. F. Smull, 2009: On how hot towers fuel the Hadley cell: An observational and modeling study of line-organized convection in the equatorial trough from TOGA COARE. *J. Atmos. Sci.,* **66,** 2730–2746.

Garstang, M. A., and C. I. Aspliden, 1974: Convective cloud code. Department of Environmental Science, University of Virginia, Charlottesville GATE International Experiment Rep., 20 pp.

Kim, D., and V. Ramanathan, 2008: Solar radiation budget and radiative forcing due to aerosols and clouds. *J. Geophys. Res.,* **113,** D02203, doi:10.1029/2007JD008434.

Kloesel, K. A., and B. A. Albrecht, 1989: Low-level inversions over the tropical Pacific—Thermodynamic structure of the boundary layer and the above-inversion moisture structure. *Mon. Wea. Rev.,* **117,** 87–101.

Knight, C. A., L. J. Miller, and R. A. Rilling, 2008: Aspects of precipitation development in trade wind cumulus revealed by differential reflectivity at S band. *J. Atmos. Sci.,* **65,** 2563–2580.

Malkus, J. S., 1958: On the structure of the trade wind moist layer. MIT and WHOI Papers in Physical Oceanography and Meteorology, Vol. 13, No. 2, 47 pp.

Minor, H. A., R. M. Rauber, S. Göke, and L. Di Girolamo, 2011: Trade wind cloud evolution observed by polarization radar: Relationship to giant condensation nuclei concentrations and cloud organization. *J. Atmos. Sci.,* **68,** 1075–1096.

Neggers, R. A. J., A. P. Siebesma, and H. J. J. Jonker, 2002: A multiparcel model for shallow cumulus convection. *J. Atmos. Sci.,* **59,** 1655–1668.

——, H. J. J. Jonker, and A. P. Siebesma, 2003: Size statistics of cumulus cloud populations in large-eddy simulations. *J. Atmos. Sci.,* **60,** 1060–1074.

——, B. Stevens, and J. D. Neelin, 2006: A simple equilibrium model for shallow cumulus topped mixed layers. *Theor. Comput. Fluid Dyn.,* **20,** 305–322, doi:10.1007/s00162-006-0030-1.

Nitta, T., and S. Esbensen, 1974: Diurnal variations in the Western Atlantic trades during the BOMEX. *J. Meteor. Soc. Japan,* **52,** 254–257.

Nuijens, L., B. Stevens, and A. P. Siebesma, 2009: The environment of precipitating shallow cumulus convection. *J. Atmos. Sci.,* **66,** 1962–1979.

Pennell, W. T., and M. A. LeMone, 1974: An experimental study of turbulence structure in the fair-weather trade wind boundary layer. *J. Atmos. Sci.,* **31,** 1308–1323.

Rauber, R. M., and Coauthors, 2007: Rain in shallow cumulus over the ocean. *Bull. Amer. Meteor. Soc.,* **88,** 1912–1928.

Reiche, C. K. H., and S. G. Lasher-Trapp, 2010: The minor importance of giant aerosol to precipitation development within small trade wind cumuli observed during RICO. *Atmos. Res.,* **95,** 386–399.

Riehl, H., T. C. Yeh, J. S. Malkus, and N. E. Laseur, 1951: The northeast trade of the Pacific Ocean. *Quart. J. Roy. Meteor. Soc.,* **77,** 598–626.

Roberts, R. D., and Coauthors, 2008: REFRACTT 2006. *Bull. Amer. Meteor. Soc.,* **89,** 1535–1548.

Ruttenberg, S., 1975: *GATE Information Bulletin*. No. 8, GATE Project Office, Rockville, MD, 43 pp. [Available online at http://nldr.library.ucar.edu/repository/assets/gate/GATE-000-000-000-008.pdf.]

Siebesma, A. P., 1998: Shallow cumulus convection. *Buoyant Convection in Geophysical Flows,* E. J. Plate et al., Eds., Kluwer, 441–486.

——, and J. W. M. Cuijpers, 1995: Evaluation of parametric assumptions for shallow cumulus convection. *J. Atmos. Sci.,* **52,** 650–666.

——, and A. A. M. Holtslag, 1996: Model impacts of entrainment and detrainment rates in shallow cumulus convection. *J. Atmos. Sci.,* **53,** 2354–2364.

——, and Coauthors, 2003: A large eddy simulation intercomparison study of shallow cumulus convection. *J. Atmos. Sci.,* **60,** 1201–1219.

Snodgrass, E. R., L. Di Girolamo, and R. M. Rauber, 2009: Precipitation characteristics of trade wind clouds during RICO derived from radar, satellite, and aircraft measurements. *J. Appl. Meteor. Climatol.,* **48,** 464–483.

Sommeria, G., and M. A. LeMone, 1978: Direct testing of a three-dimensional model of the planetary boundary layer against experimental data. *J. Atmos. Sci.,* **35,** 25–39.

Stevens, B., 2005: Atmospheric moist convection. *Annu. Earth Planet. Sci.,* **32,** 605–643.

——, 2006: Bulk boundary layer concepts for simplified models of tropical dynamics. *Theor. Comput. Fluid Dyn.,* **20,** 279–304.

——, and J.-L. Brenguier, 2009: Cloud-controlling factors: Low clouds. *Clouds in the Perturbed Climate System: Their Relationship to Energy Balance, Atmospheric Dynamics, and Precipitation,* J. Heintzenberg and R. Charlson, Eds., MIT Press, 173–196.

——, and Coauthors, 2001: Simulations of trade wind cumuli under a strong inversion. *J. Atmos. Sci.,* **58,** 1870–1891.

Stull, R. B., 1988: *An Introduction to Boundary Layer Meteorology.* Kluwer Academic Publishers, 670 pp.

Trenberth, K. E., and Coauthors, 2007: Observations: Surface and atmospheric climate change. *Climate Change 2007: The Physical Science Basis,* S. Solomon et al., Eds., Cambridge University Press, 235–336.

Vaisala, 2010: Vaisala radiosonde RS-92-SGP. Vaisala Reference Doc. B210358EN-E, 2 pp. [Available online at http://www.vaisala.com/Vaisala%20Documents/Brochures%20and%20Datasheets/RS92SGP-Datasheet-B210358EN-F-LOW.pdf.]

vanZanten, M. C., and Coauthors, 2011: Controls on precipitation and cloudiness in simulations of trade-wind cumulus as observed during RICO. *J. Adv. Model. Earth Syst.,* **3,** M06001, doi:10.1029/2011MS000056.

von Salzen, K., and N. A. McFarlane, 2002: Parameterization of the bulk effects of lateral and cloud-top entrainment in transient shallow cumulus clouds. *J. Atmos. Sci.,* **59,** 1405–1430.

Währn, J., I. Rekikoski, H. Jauhiainen, and J. Hirvensalo, 2004: New Vaisala radiosonde RS92: Testing and results from the field. Preprints, *Eighth Symp. on Integrated Observing and Assimilation Systems for Atmosphere, Oceans, and Land Surface,* Seattle, WA, Amer. Meteor. Soc., 4.13. [Available

online at http://ams.confex.com/ams/84Annual/techprogram/paper_72134.htm.]

Weckwerth, T. M., and Coauthors, 2004: An overview of the International H_2O Project (IHOP_2002) and some preliminary highlights. *Bull. Amer. Meteor. Soc.,* **85,** 253–277.

Xue, H., and G. Feingold, 2006: Large-eddy simulations of trade wind cumuli: Investigation of aerosol indirect effects. *J. Atmos. Sci.,* **63,** 1605–1622.

——, ——, and B. Stevens, 2008: Aerosol effects on clouds, precipitation, and the organization of shallow cumulus convection. *J. Atmos. Sci.,* **65,** 392–406.

Yanai, M., S. Esbensen, and J. Chu, 1973: Determination of bulk properties of tropical cloud clusters from large-scale heat and moisture budgets. *J. Atmos. Sci.,* **30,** 611–627.

Yin, B., and B. Albrecht, 2000: Spatial variability of atmospheric boundary layer structure over the eastern equatorial Pacific. *J. Climate,* **13,** 1574–1592.

Yuter, S. E., and R. A. Houze, 1995: Three-dimensional kinemetic and microphysical evolution of Florida cumulonimbus. Part II: Frequency distributions of vertical velocity, reflectivity, and differential reflectivity. *Mon. Wea. Rev.,* **123,** 1941–1963.

Zhao, G., and L. Di Girolamo, 2007: Statistics on the macrophysical properties of trade wind cumuli over the tropical western Atlantic. *J. Geophys. Res.,* **112,** D10204, doi:10.1029/2006JD007371.